Microstructural Evolution of Zirconia Nanoparticles Caused by Rare-Earth Modification and Heat Treatment

C.-K. Loong,*,[1] P. Thiyagarajan,* J. W. Richardson Jr.,* M. Ozawa,† and S. Suzuki†

*Argonne National Laboratory, Argonne, Illinois 60439-4814; †Nagoya Institute of Technology, Tajimi, Gifu, 507, Japan

High-surface-area zirconias are widely used as catalytic support of noble metals or oxygen sensor electrolytes in automobile exhaust-emission-control systems. Doping zirconia with small amounts of rare-earth (RE) elements may tailor its properties for better catalytic performance. The microstructure in terms of primary-particle size, surface area, porosity, and fractal aggregates of 10 mol% RE-doped zirconias (RE = Nd and Ce) and pure ZrO_2 were characterized by nitrogen adsorption isotherm and small-angle neutron scattering measurements. The crystal phases of these powders were examined by neutron powder diffraction method. Fresh pure zirconia prepared by a hydrolysis method at low temperature consists of small ($\sim$4 nm) particles and micropores. Subsequent heat treatments induce a transformation from microporosity to mesoporosity thereby an increase of particle size and a reduction of surface area. In the case of pure ZrO_2 a crossover from a mass-fractal aggregate of rough particles to clustering of smooth particles at a heat-treatment temperature of 600°C was observed. The Nd-modified zirconias prepared by a coprecipitation method, on the other hand, show high resistance to sintering and retain a small particle size and the mass-fractal aggregate after heat treatment at 600°C. Because of the different oxidation states and ionic sizes of Nd^{3+} and Ce^{4+} ions, $Nd_{0.1}Zr_{0.9}O_{1.95}$ and $Ce_{0.1}Zr_{0.9}O_2$ powders exhibit different crystal phases, particle size distributions, and pore structure.

© 1997 Academic Press

I. INTRODUCTION

The present study is motivated by the need of better support materials for noble metals in three-way catalytic converters for automobiles. High-surface-area zirconia is one of the commonly used materials for this purpose. Doping rare-earth elements (RE) in zirconia helps stabilize the cubic and tetragonal phases over a wide range of temperatures thereby removing the disruptive phase transformations in pure zirconia (1). The resulting RE-Zr oxide system shows a robust thermal stability that is desirable for catalytic applications. Depending on the valency of the dopant RE ions

(e.g., Nd^{3+} or Ce^{4+} versus Zr^{4+}), ionic charge compensation may lead to oxygen vacancies in the crystalline solid solution. The diffusion of oxygen ions via vacancy sites under an oxygen pressure gradient can provide an additional handle in tailoring the electronic response of an oxygen sensor and the oxygen storage capacity of an air-purification catalyst. In particular, CeO_2 is thought to promote the oxidation reaction of carbon monoxide (CO) and hydrocarbons (HC) as well as the deoxidization reaction of nitric oxide (NO_x) via a dynamic change of the Ce oxidation states during a catalytic cycle (2–5). In general, rare-earth impurities modify the interfacial energies, diffusion coefficients, and crystalline anisotropy in a complex manner. As a result, the porosity, particle-size distribution, and resistance to sintering vary depending on the dopant element, the preparation method, and processing. Clearly, a complete understanding of these phenomena requires systematic investigations by many different methods.

In a previous study of RE_2O_3-ZrO_2 powders of RE compositions up to 50 mol%, the effects of heat treatment on the crystal morphology and thermal stability were characterized over the 600–1200°C temperature range (6). Here we concentrate on a detailed study of the microstructure of pure ZrO_2 and Ce- and Nd-doped zirconias at lower annealing temperatures that are typical to the operation of three-way catalytic converters. A relatively low RE doping (10 mol%) is chosen in this first study so that the materials will not be complicated by the formation of intermediate phases (7). We have applied the methods of small-angle neutron scattering (SANS) and nitrogen adsorption to characterize the microstructure of a pure zirconia powder prepared by a hydrolysis method and two RE-modified zirconia powders, $Nd_{0.1}Zr_{0.9}O_{1.05}$ and $Ce_{0.1}Zr_{0.9}O_2$, prepared by a coprecipitation method. The crystal structures were examined by neutron powder diffraction (NPD). The powders were subjected to *ex situ* and *in situ* heat treatments up to 800°C during the investigation. We report the crystal phases, surface areas, pore and particle size distributions, and self-similar behavior of these powders as a function of heat-treatment temperatures.

[1] Person to whom correspondence should be mailed. E-mail: ckloong@anl.gov.

II. EXPERIMENTAL DETAILS

1. Sample Preparation

The pure zirconia powder was synthesized from hydrolysis of a 0.3 mol% $ZrOCl_2$ aqueous solution at 100°C for 91 h. The sediment obtained from filtration was washed and freeze-dried. The powder was subsequently heated at 290°C in air for 3 h. An X-ray diffraction study qualitatively confirmed the monoclinic structure of fine ZrO_2 crystalline particles. The fresh powder was divided into two batches. One batch was used for *in situ* SANS experiments. The other batch was subjected to sequential heat treatments at 400, 500, 600, 700, and 800°C in air, each for about 3 h. After each heat treatment a sample was taken out for NPD and SANS measurements at room temperature.

The 10 mol% RE-modified zirconia (RE = Nd and Ce) powders were prepared by a coprecipitation technique. Mixtures of hydrous zirconium and rare earth were coprecipitated from an agitated aqueous solution of $ZrOCl_2$ and $RECl_3$ (total concentration of 0.8 mol^{-1} at the final pH value of 10) with excess of 10 wt% NH_4OH solution. The products were filtered and washed with distilled water and then dried by a supercritical technique. The dried mixtures were calcined at 600°C in air for 3 h. Details concerning the preparation and characterization of the RE-modified zirconias have been given elsewhere (6).

2. Neutron Powder Diffraction and Small-Angle Scattering

Neutron powder diffraction experiments were carried out using the General Purpose Powder Diffractometer (GPPD) at the Intense Pulsed Neutron Source (IPNS) of Argonne National Laboratory. A powder sample was enclosed in a thin-wall vanadium can (11-mm diameter, 50-mm long) for room-temperature measurements. A resolution of $\triangle d/d = 0.25\%$ (where d is the atomic spacing) can be achieved from a backscattering geometry at a mean scattering angle (2θ) of $\pm148°$. For the present zirconia samples with small grains, resolution effect is not a limiting factor to data analysis.

While conventional powder diffraction yields information regarding the average structure of atomic organization over a length scale of typically a crystalline unit-cell dimension, small-angle scattering provides a characterization of inhomogeneity up to ~100 nm. The scattering at low wavevector, $Q = 4\pi \sin\theta/\lambda$ (where θ is the scattering angle and λ is the neutron wavelength) arises from fluctuations of neutron-scattering cross section in the sample. In the present case the scattering contrast comes from the zirconia particles versus the pores. The SANS experiments were carried out using the small-angle diffractometers, SAD, and SAND at IPNS. Incident neutrons with wavelengths in the range of 0.05–1.4 nm were used and the sample-to-detector distance of 1.54 m was fixed throughout the experiment.

The scattered neutron intensities as a function of position and time were recorded by using a gas-filled area detector and time-of-flight techniques. The sample was enclosed in a Suprasil cell (sample thickness 2 mm) and controlled at a temperature between ambient temperature and 500°C. The data were corrected for background and empty-cell scattering, as well as detector nonlinearity, and were normalized by using the known scattering cross section of a silica gel standard. A good Q-resolution (root-mean-square deviation varying from about 0.001 to 0.012 Å^{-1} over the observed Q-range of 0.007–0.03 Å^{-1}) was achieved without altering the sample-to-detector configuration. We find no noticeable effect of instrumental resolution on the interpretation of the present data. Details about the small-angle diffractometers were given elsewhere(8).

3. Nitrogen Adsorption Isotherm Measurements

The adsorption–desorption isotherms of nitrogen at 77 K were measured with the apparatus Autosorb (Quantachrome, USA) as a function of relative pressure P/P_0 over the range of 0.01–0.99. Prior to the a measurement, the sample was outgassed at $\sim150°C$ under vacuum for 8 h. Pore volume was estimated from nitrogen uptake at $P/P_0 \approx 0.99$.

III. EXPERIMENTAL RESULTS

1. Powder Diffraction

Pure ZrO_2 has three polymorphs: a cubic fluorite structure (space group Fm3m) above 2640 K, a tetragonal structure (P4$_2$/nmc) between 1400 and 2640 K, and a monoclinic structure (P2$_1$/c) below 1400 K. A small amount of rare-earth solutes in zirconia can stabilize the tetragonal and cubic phases over a wide range of temperatures (1, 6). Figure 1 displays a portion of the observed, background-subtracted, and fitted powder patterns of the $Nd_{0.1}Zr_{0.9}O_{1.95}$ and $Ce_{0.1}Zr_{0.9}O_2$ that were heat treated at 600°C. First, the NPD patterns clearly show different crystal structures for the two samples: a mixture of cubic and tetragonal phases in the $Nd_{0.1}Zr_{0.9}O_{1.95}$ and a tetragonal structure in $Ce_{0.1}Zr_{0.9}O_2$. Second, the broad Bragg peaks indicate a small average crystallite size in both materials. Third, the oscillatory residual intensities in $Nd_{0.1}Zr_{0.9}O_{1.95}$ and the anomalous peak profiles in $Ce_{0.1}Zr_{0.9}O_2$ underscore the short-range defect structures in RE-modified ZrO_2.

The NPD profiles of the pure zirconia after annealing at 290 (as prepared), 400, 500, 600, and 700°C are shown in Fig. 2. First, all the patterns show the monoclinic crystal structure as expected for ZrO_2. Second, the peaks sharpen progressively with increasing annealing temperature, indicating a continuing grain growth and relaxation of internal microstrain. Third, a broad Lorentzian-like component in the peak profiles similar to that in $Ce_{0.1}Zr_{0.9}O_2$ was observed. The observed peaks in the sample heat treated at
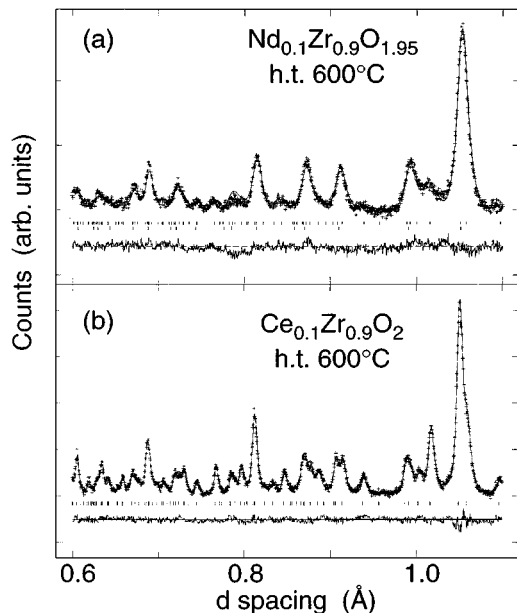
FIG. 1. Rietveld profile fits in the 0.6 to 1.1-Å region of *d*-spacing for (a) $Nd_{0.1}Zr_{0.9}O_{1.95}$ and (b) $Ce_{0.1}Zr_{0.9}O_2$ powders that were subjected to heat treatment at 600°C. The dots are the observed, background-subtracted intensities. The solid line represents the calculated crystalline intensities. Tick marks indicate the positions of the Bragg reflections: in (a) cubic (top row) and tetragonal (bottom row) phases, and in (b) tetragonal phase. The residual intensities before Fourier filtering are shown at the bottom of each panel where oscillatory deviations are evident in $Nd_{0.1}Zr_{0.9}O_{1.95}$.

700°C are still much wider than the corresponding ones in a commercial ZrO_2 powder prepared by high-temperature (>900°C) techniques. Therefore, one expects continuing grain growth at higher annealing temperatures.

2. Small-Angle Scattering

Figure 3 shows the SANS data in terms of log-intensity versus log-Q profiles taken at ambient temperature for $Nd_{0.1}Zr_{0.9}O_{1.95}$, $Ce_{0.1}Zr_{0.9}O_2$, and ZrO_2 that were heat-treated at 600°C. First, the intensity profiles of the three samples show distinct Q-dependence, which implies RE-dopant specific microstructural changes induced by the modification. Second, each profile shows a break at a certain Q (denoted by an arrow in Fig. 3) which roughly marks a change of slope in the curve. The position of this breaking point shifts progressively to lower Q for $Nd_{0.1}Zr_{0.9}O_{1.95}$, $Ce_{0.1}Zr_{0.9}O_2$, and ZrO_2, which implies a corresponding increasing mean particle size (see the next section). Figure 4 shows the evolution of the SANS profiles of pure ZrO_2 subjected to *ex situ* heat treatments from 290 to 800°C. Again, a progressive change in the particle size and porosity resulting from annealing was observed.

3. Nitrogen Adsorption Isotherms

The isotherms of both $Ce_{0.1}Zr_{0.9}O_2$ and $Nd_{0.1}Zr_{0.9}O_{1.95}$ exhibit a shape of Type IV with a Type A hysteresis loop, as shown in Fig. 5. This is characteristic of mesoporosity
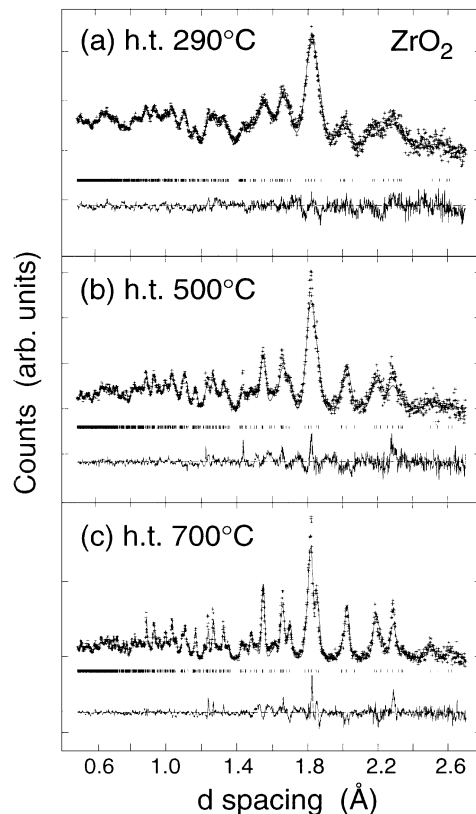

FIG. 2. Rietveld profile fits in the 0.5 to 2.7-Å region of *d*-spacing for pure ZrO_2 samples at selected heat-treatment temperatures: (a) 290, (b) 500, and (c) 700°C. The dots and solid lines represent the observed, background subtracted intensities, and the calculated crystalline intensities, respectively.
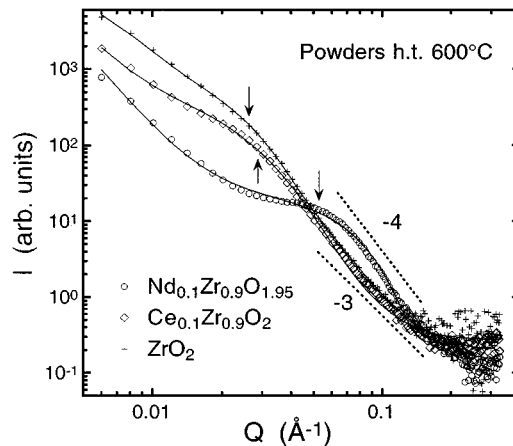

FIG. 3. The log–log plot of SANS intensity versus Q for $Nd_{0.1}Zr_{0.9}O_{1.95}$, $Ce_{0.1}Zr_{0.9}O_2$, and ZrO_2 that were heat-treated at 600°C. Typical errors are of the size of the symbols, except for $Q > 0.1$ Å^{-1} where errors are large. The solid lines represent the fits of the data to the fractal model. Limiting slopes for power-law behavior are given by the dotted lines (see text).
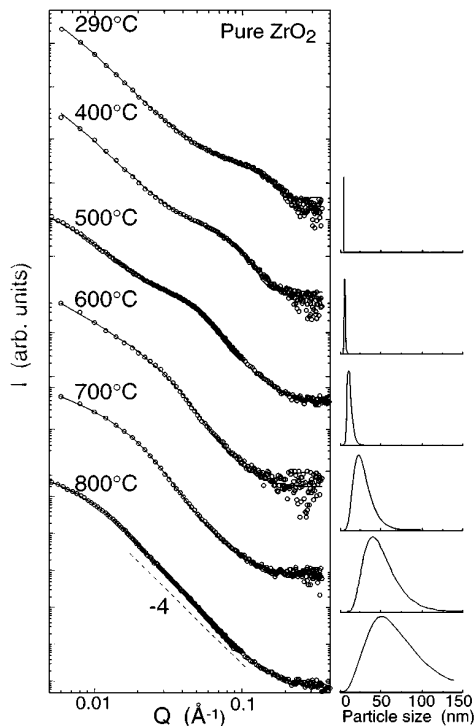
FIG. 4. The log–log plot of SANS data for pure ZrO_2. All data were collected using the SAD instrument except for the data sets for 500 and 800°C annealing which were obtained from the SAND instrument. The SAND diffractometer equipped with an area detector larger than that of SAD thereby providing data over a wider Q-range. The solid lines for annealing temperatures equal to or below 500°C are fits of the data using the fractal model whereas those for other temperatures are fits using the Ornstein–Zernike model. The dashed line represents power-law behavior of slope −4. The plots on the right display the particle size distributions corresponding to different annealing temperatures.

FIG. 6. The pore-volume ln radius distribution function of the heat-treated $Nd_{0.1}Zr_{0.9}O_{1.95}$, $Ce_{0.1}Zr_{0.9}O_2$ obtained from a t-plot analysis.

with principally open-ended cylindrical pores (9). The hysteresis loop of $Ce_{0.1}Zr_{0.9}O_2$ occurs at higher relative pressures than those of $Nd_{0.1}Zr_{0.9}O_{1.95}$, which is indicative of a larger average pore radius in $Ce_{0.1}Zr_{0.9}O_2$. The uptake of adsorption at a characteristic relative pressure (∼0.6 and
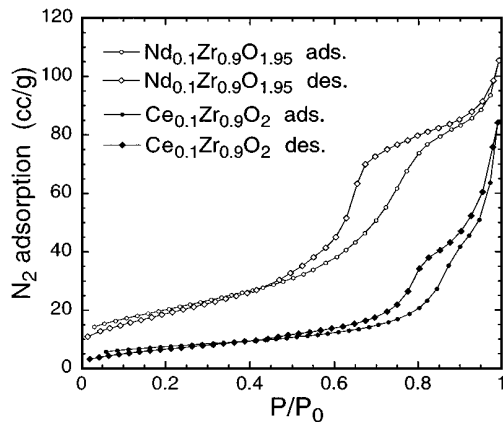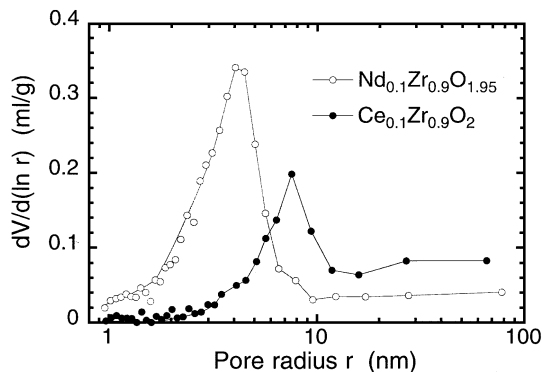
∼0.75 for $Ce_{0.1}Zr_{0.9}O_2$ and $Nd_{0.1}Zr_{0.9}O_{1.95}$, respectively) in the isotherms signifies multilayer condensation of nitrogen in the mesopores. At low pressure, the isotherms display the characteristic of monolayer adsorption on micropores which are formed between tightly bound crystalline grains. This behavior is common to zirconia powders prepared using aqueous solutions and subsequently dried at a low temperature (10–12). A t-plot analysis of the pore-size distribution, as shown in Fig. 6, reveals that the rare-earth modified powders consist of principally mesopores which are present within aggregates of primary and secondary particles.

The isotherms of pure ZrO_2 heat treated at 290°C (as prepared) and 600°C, as shown in Fig. 7, exhibit Type II behavior (9). The effect of heat treatment on the porosity of the powders can be seen from the curves of pore-size distribution as shown in Fig. 8. While the as-prepared sample contains a considerable amount of micropores in addition to macropores, the heat-treated sample is devoid of microporosity. Consequently, the 600°C-heat-treated pure ZrO_2 powder show a considerably smaller surface area and larger pore volume than those of the as prepared powder.

FIG. 5. Nitrogen adsorption–desorption isotherms at 77 K for $Nd_{0.1}Zr_{0.9}O_{1.95}$, $Ce_{0.1}Zr_{0.9}O_2$ that were heat treated at 600°C.
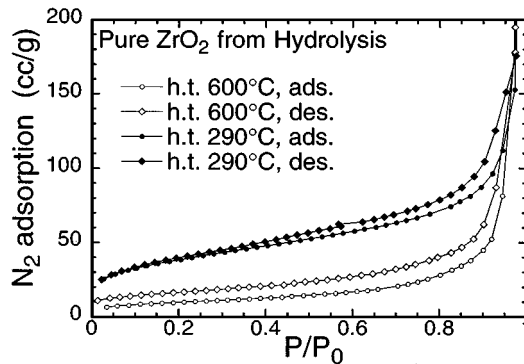

FIG. 7. Nitrogen adsorption–desorption isotherms at 77 K for pure ZrO_2 that were heat treated at 290 and 600°C.
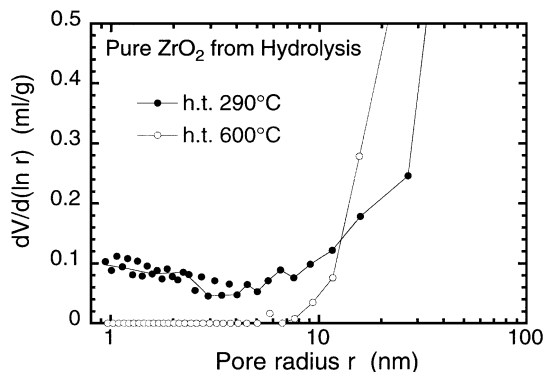
FIG. 8. The pore-volume ln radius distribution function of the pure ZrO_2 powders obtained from a t-plot analysis.

IV. DISCUSSION

Experimental results from neutron scattering and N_2 adsorption studies show evidence of different crystal phases and microstructures of zirconia powders that are subjected to rare-earth modification and heat treatment. We now present a quantitative analysis of the data. The NPD profiles were analyzed by the Rietveld profile refinement method (13). In general, Bragg diffraction arises from coherent scattering of neutrons by long-range atomic order in the crystalline grains averaged over the sample. Incoherence among the crystalline grains, such as distribution of grain sizes, grain boundaries, and microstrains, causes deviations in the observed Bragg-peak intensities from those expected for an ideal powder. Within the Rietveld refinement some of these effects such as the average grain size and mircrostrain

can be modeled by adjustable parameters (14). Short-range atomic disorder such as defects, compositional fluctuations, atomic displacements from lattice sites, on the other hand, give rise to another type of coherent scattering which may be manifest as a diffuse, variant component superimposed on the Bragg scattering. Some features of the short-range order structures may be revealed in terms of a real-space correlation function which can be extracted from a Fourier filtering analysis. However, if several substructures coexist, as in the present zirconia samples, interpretation of the diffraction results should be treated with caution.

While the crystal structure of heat-treated pure ZrO_2 remains monoclinic, the $Ce_{0.1}Zr_{0.9}O_2$ and $Nd_{0.1}Zr_{0.9}O_{1.95}$ powders exhibit crystal structures characteristic of stabilized high-temperature phases of pure zirconia, i.e., a mixture of cubic (58.7% mole fraction) and tetragonal (41.3%) in the $Nd_{0.1}Zr_{0.9}O_{1.95}$ and a tetragonal structure in $Ce_{0.1}Zr_{0.9}O_2$. This can be seen from the satisfactory refinements (weighted R-factors 4–10%) shown in Figs. 1 and 2. In the analysis of the peak profiles we find an adequate representation of all the data by assuming a superposition of a Gaussian and a Lorentzian component from which the average crystalline grain size and microstrains were estimated, respectively. The results are listed in Table 1. As expected, the particle size of pure ZrO_2 increases with increasing heat-treatment temperature. As the particles coarsen, the strain in the crystalline lattice is released considerably.

In $Nd_{0.1}Zr_{0.9}O_{1.95}$ ionic charge compensation for the different oxidation states of Nd(III) and Zr(IV) cations in the lattice results in oxygen vacancies. The data were analyzed by assuming a random substitution of Zr with Nd and

TABLE 1

Parameters Characteristic of the Crystal Phases and Microstructures of Rare-Earth-Modified and Pure Zirconia Powders[a]

Parameters	$Nd_{0.1}Zr_{0.9}O_{1.95}$ h.t. 600°C	$Ce_{0.1}Zr_{0.9}O_2$ h.t. 600°C	ZrO_2 h.t. 290°C	ZrO_2 h.t. 400°C	ZrO_2 h.t. 500°C	ZrO_2 h.t. 600°C	ZrO_2 h.t. 700°C	ZrO_2 h.t. 800°C
Preparation method	Coprecipitation	Coprecipitation	Hydrolysis	Hydrolysis	Hydrolysis	Hydrolysis	Hydrolysis	Hydrolysis
Crystal structure	Cubic/tetragonal	Tetragonal	Monoclinic	Monoclinic	Monoclinic	Monoclinic	Monoclinic	Monoclinic
Crystalline grain size (nm)	20.2(7)/8.8(2)	39.1(11)	6.3(2)	10.5(12)	15.5(7)	20.8(8)	27.4(11)	
Microstrain (%)	0.43(4)/0.67(4)	0.53(1)	2.16(7)	2.16(11)	1.35(3)	0.90(2)	0.66(3)	
Weighted R (%)	5.6	6.6	3.9	9.4	7.7	8.1	8.2	
Primary-particle size (nm)	6.56(1)	20.6(1)	3.62(3)	5.68(2)	11.2(4)	22.8(8)	40.1(9)	68.4(25)
Size distribution r.m.s. deviation	1.17(2)	1.44(2)	1.05(2)	1.12(2)	1.32(2)	1.49(2)	1.50(2)	1.57(2)
Fractal cutoff (nm)	575(15)	500(20)	26.1(4)	26.4(3)	22.0(2)			
Fractal dimension	2.97(2)	2.92(2)	2.31(4)	2.84(1)	2.82(2)			
Surface area (m²/g)	72.3	26.1	135.4			35.1		
Pore volume (ml/g)	0.163	0.130	0.856			2.51		
Pore radius (nm)	∼3	∼5	Microporous			Macroporous		

[a] The mean crystalline grain size and microstrain were estimated from the Gaussian and Lorentzian components of the fitted diffraction peak profiles, respectively. The primary-particle size and its distribution were obtained from fitting the small-angle scattering data with the fractal model ($Nd_{0.1}Zr_{0.9}O_{1.95}$, $Ce_{0.1}Zr_{0.9}O_2$, and ZrO_2 h.t. ≤ 500°C) and with the Orenstein–Zernike model (ZrO_2 h.t. ≥ 600°C). The specific area and porosity were obtained from BET and t-plot analysis of the N_2 adsorption data.

an oxygen deficiency of 5 mol%. Although all the Bragg peaks are accounted for by the two-phase crystal structure, a broad, oscillatory deviation from the calculated crystalline profile is evident in the residual profile in Fig. 1a. This oscillatory component was fitted by a smooth, long period background function (related to the real space correlation function) thereby filtering out the sharp features due to crystalline contributions. Interpretation of coefficients in the background function corresponding to short-range interatomic spacings, revealed evidence of static, oxygen vacancy-induced atomic displacements along the pseudocubic $\langle 111 \rangle$ and other directions. Similar results were also found in a 10 mol% lanthanum doped sample, $La_{0.1}Zr_{0.9}O_{1.95}$ (15). Such a procedure led to significant improvement of the fit. The same Fourier filtering analysis was performed on the Ce(IV)-doped zirconia spectra but no obvious spatial correlations due to atomic displacements were found. The fit was made according to a fully stoichiometric oxygen occupancy.

The structure of ramified objects formed by aggregates of small particles has been studied extensively by a variety of experimental methods including small-angle scattering (10, 16–27). The present study focuses on the characterization of the crystalline powders rather than the sol-gels since nominally anhydrous polycrystalline materials are employed for catalytic applications as support components. A characterization of the size distribution of the constituent particles and the porous structure according to sample preparation routes and processing conditions (e.g., heat treatments) is of crucial importance. SANS permits a measurement of the local density of an aggregate as a function of length scale. The observed intensity can be expressed as a product of the form factor of the particles, $P(Q)$, and the interparticle structure factor, $S(Q)$,

$$I(Q) \propto P(Q)S(Q). \quad [1]$$

Our method of analysis of the SANS data was governed by the following criteria: (1) quantitative information regarding the particle size and its distribution, as well as the nature of the aggregate in terms of interparticle correlation can be obtained; (2) the models employed can be applied to interpret the data over the entire Q-range; and (3) introduction of adjustable parameters which do not significantly affect the quality of the fits is avoided. We used the form factor for a spherical particle of radius R, volume V, and scattering-length density ρ, as evidenced in electron microscopic studies (6, 28),

$$P(Q) = V^2(\rho - \rho_0)^2 \left[3 \frac{\sin(QR) - QR\cos(QR)}{(QR)^3} \right]^2. \quad [2]$$

For the structure factor, which is related to the spatial pair-correlation function of the particles through a Fourier transform, we adopted the $S(Q)$ for a mass fractal as was used in previous studies of porous materials, aggregates, and col-

loidal systems (25, 29). By definition a mass fractal having a fractal dimension D, namely, the total mass inside a distance r scales as $M \propto r^D$, a pair-correlation function can be constructed as

$$g(r) = \frac{D}{4\pi} \frac{1}{R^D} r^{D-3} \exp(-r/\xi) + 1, \quad [3]$$

where ξ is a cutoff distance beyond which the density of the fractal object approaches the macroscopic density. The structure factor then becomes (25, 29)

$$S(Q) = 1 + \frac{1}{(QR)^D} \frac{D\Gamma(D-1)}{\left(1 + \frac{1}{Q^2\xi^2}\right)^{(D-1)/2}} \sin[(D-1)\arctan(Q\xi)], \quad [4]$$

where $\Gamma(x)$ is a gamma function. One of the goals is to estimate the mean particle size ($\sim 2R$) and the size distribution in the zirconia powders. Therefore, the expression in Eq. [1] was integrated over a log-normal distribution of sizes with a geometric standard deviation σ (30). σ is a dimensionless variable equal to the ratio of the particle size at 15.87% probability to the geometric mean particle size at 50% probability. Hence $\sigma = 1$ implies a distribution of uniform size (monodispersity). The SANS data were fitted using Eqs. [1], [2], and [4] which contain six adjustable parameters: R, σ, ξ, D, a prefactor in Eq. [1], and a Q-independent background.

As can be seen in Fig. 3 the distinct SANS profiles of heat-treated $Nd_{0.1}Zr_{0.9}O_{1.95}$ and $Ce_{0.1}Zr_{0.9}O_2$ and pure ZrO_2 at $600°C$ can be described adequately by the fractal model. In general, the position of the broad maximum is mainly determined by the particle form factor from which the mean particle size ($2R$) and size distribution (in terms of σ) can be extracted reliably. The best fits of the data suggest values of ($2R, \sigma$) for the Nd-doped, Ce-doped, and pure zirconia to be (6.56, 1.17), (20.6, 1.44), and (22.8, 1.49), respectively. This result indicates that doping Nd(III) ions in ZrO_2 is more effective in preserving the small particle size and the large surface area of the powder. This in part is due to the larger ionic radius of Nd^{3+} (0.098 nm) than that of Ce^{4+} (0.080 nm) and Zr^{4+} (0.072 nm) (31, 32) which hinders diffusion of atoms from sintering into larger particles. The mass-fractal dimension and cutoff distance (D, ξ), on the other hand, depend mainly on the shape and slope of the curve in the Guinier region ($QR \cong 1$). For samples having identical particle size the initial slopes of the curves in a log-I versus log-Q plot may be used to estimate the fractal dimensions. However, for samples having different particle size and polydispersity, as in the present case, such a method of determination of the fractal dimension is not warranted. The fractal dimension and cutoff distance (D, ξ) for the Nd-doped, Ce-doped, and pure zirconia were found to be (2.97, 575 nm), (2.92, 500 nm), and (2.64, 21.2 nm), respectively. A fundamental property of fractal objects is self-affinity over the characteristic fractal length scale. This implies $\xi \gg R$. This behavior is confirmed in the Nd-doped

and Ce-doped zirconia, but not in the pure zirconia that are heat treated at 600°C. Therefore, although the fractal model provides a good fit to the ZrO$_2$ data, the fractal interpretation is not a physical one. In fact, we find that a crossover from a mass-fractal assembly to clusters of solid particles occurs in pure zirconia at a heat-treatment temperature about 600°C (see below). The final parameters and estimated uncertainties from the fits are given in Table 1.

The fractal model describes very well the data of pure ZrO$_2$ up to the heat-treatment temperature of 500°C (see Fig. 4). As the samples were annealed from 290 to 500°C, the mean particle size increased from ∼3.62 nm to ∼11.2 nm, and the size distribution expanded from $\sigma = 1.05$ to $\sigma = 1.32$. The fractal dimension did not change significantly but the fractal cutoff distance decreased from 26.1 nm to 22.0 nm. The result reflects the microstructural change of the powders due to sintering at elevated temperatures. At higher temperatures, although the fractal model provided a good fit to the data and confirmed the trend of particle coarsening, the fractal dimensions and cutoff distances no longer made physical sense. This suggests that the particles have grown in size to an extent that self-affinity behavior cannot be sustained over an increasing length scale. Instead, the assembly is better described as a random packing of solid particles with intertwining macroporosity. We find that an excellent description of the high-temperature data was achieved by using the Ornstein–Zernike-type model (33, 34),

$$S(Q) = 1 + \frac{\chi}{1 + Q^2 \xi'^2}, \qquad [5]$$

where χ is a parameter related to osmotic compressibility in the case of liquids system and ξ' is the correlation length of the clusters. It can be seen from Fig. 4 that this model fits the data above 500°C annealing temperature very well. The particle size and polydispersity, $(2R, \sigma)$ for 600, 700, and 800°C heat-treated samples are (22.8, 1.49), (40.1, 1.50), and (68.4, 1.57), respectively, and are similar to those obtained from fitting the fractal model. However, the Ornstein–Zernike model failed to provide an adequate fit of the data for pure zirconia of annealing temperatures below 600°C and for the rare-earth modified zirconias. The complete results are given in Table 1. We also attempted to fit the high-temperature data using other models, such as the Debye–Anderson–Brumberger expression (35, 36) and the hard-sphere approximation (37, 38). They either fit the data poorly or necessitate the use additional parameters of little physical significance.

The slope of the curve over the Porod regime ($QR \gg 1$) in a log-I versus log-Q plot provides a measure of the surface roughness of the constituent particles in an aggregate. A slope of −4 indicates a smooth surface and a value between −3 and −4 implies a rough fractal-like surface (18, 29). Because of the varying and limited Q-range among data sets in the high-Q region, we find that a simple fit of
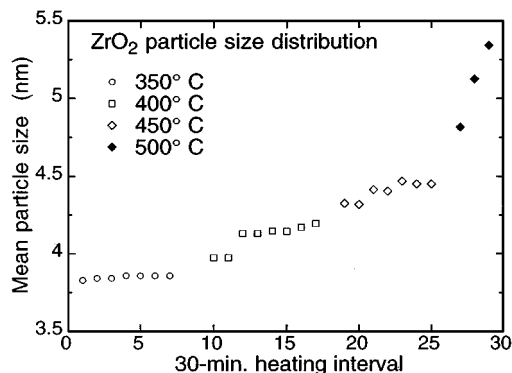

FIG. 9. The mean particle size of ZrO$_2$ deduced from *in situ* SANS measurements during heating. Each data set was collected over a 30-min interval.

the data to a power law does not warrant an accurate determination of the slopes. It can be seen from Figs. 3 and 4 that the slopes for the three powders heat-treated at or below 600°C vary between −3 and −4. This suggests a certain degree of surface roughness of particles within the micro- and mesoporous microstructure. A slope approaching −4 over a larger Q-range for pure zirconia heat-treated above 600°C (see Fig. 4), on the other hand, suggests the formation of larger and smoother particles resulted from sintering.

Finally, we tried to study the kinetics of particle coarsening over the temperature range of 350 to 500°C by *in situ* annealing. SANS data were collected in 30-min intervals as a fresh pure ZrO$_2$ powder was heated to 350, 400, 450, and 500°C. The mean particle size obtained from fits to the fractal model is displayed in Fig. 9. It shows qualitatively a slow growth of particle size between 400 and 450°C and a faster growth at 500°C. The observed sizes in the *in situ* heating are less than those from accumulative *ex situ* heat treatments (see Table 1). This suggests that particle growth over a 15-h-period did not reach the equilibrium stage.

In general, the SANS data are corroborated by the results of adsorption isotherm and NPD measurements. On the other hand, different experimental techniques probe different aspects of the microstructure and the resulting parameters need not be identical. For example, the crystalline grain size obtained from NPD represents the coherency of atomic long-range order of a global crystal structure whereas the particle size obtained from SANS represents the average size of the primary particles in the aggregate. It can been seen from Table 1 that below the annealing temperature of 600°C the crystalline grains are larger than the primary particles which were nucleated from the hydrolyzed solution. Bleier and Cannon (39) reported that the effects of hydrated Stern layers associated with complexation of zirconyl chloride tetramers may retard the growth of the primary particles, resulting in crystallite alignment during precipitation. Our NPD results suggest the presence of orientational coherency among the crystalline primary

particles. BET analysis of nitrogen adsorption measurements indicate that the high surface area of the as prepared pure ZrO_2 powders (135.4 m^2/g) is mainly due to internal surfaces of micropores within the aggregate of very small particles. As annealing temperature increases up to about 500°C, microporosity evolves to mesoporosity as particles grow in size and in size distribution. Above 500°C a more abrupt change of the microstructure occurs which leads to a crossover from a mass-fractal-like aggregate to a random packing of solid particles featuring reduced surface area and macroporosity. Apparently, this latter stage of particle growth does not lead to substantial crystalline grain-growth, as can be seen from the smaller grain sizes obtained from NPD results (Table 1). Doping Nd(III) ions in zirconia improve the ability of preserving the relatively small particle size, the mesoporosity, and high surface area at high (600°C) annealing temperature (see Fig. 5). Because of the different charge-compensation effects and ionic size between Nd^{3+} and Ce^{4+} ions in the host lattice, $Nd_{0.1}Zr_{0.9}O_{1.95}$ and $Ce_{0.1}Zr_{0.9}O_2$ exhibit distinct crystal phases and microstructure, as evidenced also from the NPD data (Fig. 1).

V. CONCLUSION

Neutron powder diffraction, small-angle neutron scattering, and N_2 adsorption isotherm measurements were carried out to characterize the crystal phases and microstructural changes of zirconia nanopowders subject to Nd- and Ce-doping and heat treatments. As-prepared pure ZrO_2 samples dried at 290°C exhibit microporosity and high surface area. Subsequent heat treatment rapidly converts microporous structure to mesoporosity. Below a heat-treatment temperature of 600°C the nature of the aggregate can be understood quantitatively as a mass-fractal. At about 600°C, however, the aggregate transforms from fractal-like to random packing of well-grown, relatively smooth particles which resulted in a large reduction of surface area due to the collapse of mesopores to a macroporous structure. The Nd- and Ce-modified zirconia, on the other hand, retain the fractal geometry and mesoporosity after annealing at 600°C. Substituting Zr with ~10 mol% of Nd to form a solid solution of rare-earth oxide and zirconia retards particle sintering and preserves the large surface area and thermal stability needed for catalytic functions.

REFERENCES

1. Green, D. J., Hannink, R. H. J., and Swain, M. V., "Transformation Toughening of Ceramics," CRC Press, Boca Raton, FL, 1989.
2. Fornasiero, P., Di Monte, R., Rao, G. R., Kaspar, J., Meriani, S., Trovarelli, A., and Graziani, M., *J. Catal.* **151**, 168 (1995).
3. Lööf, P., Kasemo, B., and Keck, K.-E., *J. Catal.* **118**, 339 (1989).
4. Ozawa, M., Kimura, M., and Isogai., A., *J. Alloys Compounds* **193**, 73 (1993).
5. Yao, H. C., and Yao, Y. F. Y., *J. Catal.* **86**, 254 (1984).
6. Ozawa, M., and Kimura, M., *J. Less-Common Metals* **171**, 195 (1991).
7. Meriani, S., and Spinolo, G., *Powder Diffr.* **2**, 255 (1987).
8. Thiyagarajan, P., Epperson, J. E., Crawford, R. K., Carpenter, J. M., Klippert, T. E., and Wozniak, D. G., *J. Appl. Cryst.* **30**, 208 (1997).
9. Gregg, S. J., and Sing, K. S. W., "Adsorption, surface area and porosity," 2nd ed. Academic Press, London, 1982.
10. Ramsay, J. D. F., Russell, P. J., and Swanton, S. W., *in* "Characterization of Porous Solids II" (F. Rodriguez-Reinoso, J. Rouquerol, K. S. W. Sing, and K. K. Unger, Eds.), p. 257. Elsevier Science, Amsterdam, 1991.
11. Lecloux, A. J., Blacher, S., Kessels, P.-Y., Marchot, P., Merlo, J.-L., Noville, F., and Rirard, J. P., *in* "Characterization of Porous Solids II" (F. Rodríguez-Reinoso, Ed.), p. 659. Elsevier Science, Amsterdam, 1991.
12. Avery, R. G., and Ramsay, J. D. F., *J. Coll. Int. Sci.* **42**, 597 (1973).
13. Richardson, J. W., Jr., and Faber, J., Jr., *Adv. X-ray Anal.* **29**, 143 (1985).
14. Klug, H. P., and Alexander, L. E., "X-ray Diffraction Procedures for Polycrystalline and Amorphous Materials," 2nd ed. Wiley, New York, 1974.
15. Loong, C.-K., Richardson, J. W., Jr., and Ozawa, M., *J. Catal.* **157**, 636 (1995).
16. Rubio, F., Rubio, J., and Oteo, J. L., *J. Mat. Sci.* **16**, 49 (1997).
17. Zeng, Y. W., Riello, P., Benedetti, A., and Fagherazzi, G., *J. Non-Cryst. Solids* **185**, 78 (1995).
18. Wong, P.-Z., and Bray, A., *J. Appl. Cryst.* **21**, 786 (1988).
19. Vacher, R., Woignier, T., and Pelous, J., *Phys. Rev. B* **37**, 6500 (1988).
20. Hurd, A., and Flower, W. L., *J. Coll. Int. Sci.* **122**, 178 (1988).
21. Bale, H. D., and Schmidt, P. W., *Phys. Rev. Lett.* **53**, 596 (1984).
22. Schaefer, D. W., Brinker, C. J., Wilcoxon, J. P., Wu, D.-Q., Phillips, J. C., and Chu, B., *Mat. Res. Soc. Symp. Proc.* **121**, 691 (1988).
23. Sinha, S. K., *Physica D* **38**, 310 (1989).
24. Teixeira, J., *J. Appl. Cryst.* **21**, 781 (1988).
25. Sinha, S. K., Freltoft, T., and Kjems, J., *in* "Kinetics of Aggregation and Gelation" (F. Family and D. P. Landau, Eds.), p. 87. Elsevier Science, Amsterdam, 1984.
26. Nicolai, T., Durand, D., and Gimel, J.-C., *in* "Light Scattering" (W. Brown, Ed.), p. 201. Oxford Univ. Press, Oxford, 1996.
27. Freltoft, T., Kjems, J. K., and Sinha, S. K., *Phys. Rev. B* **33**, 269 (1986).
28. Porod, G., *in* "Small Angle X-Ray Scattering" (O. Glatter and O. Kratky, Eds.), p. 17. Academic Press, New York, 1982.
29. Teixeira, J., *in* "On Growth and Form, Factal and Non-fractal Patters in Physics" (H. E. Stanley and N. Ostrowsky, Eds.), p. 145. Nijhoff, Dordrecht, 1986.
30. Irani, R. R., and Callis, C. F., "Particle Size: Measurement, Interpretation, and Application." Wiley, New York, 1963.
31. Shannon, R. D., and Prewitt, C. T., *Acta Cryst. B* **25**, 925 (1969).
32. Shannon, R. D., and Prewitt, C. T., *Acta Cryst. B* **26**, 1046 (1970).
33. Zemb, T. N., Hyde, S. T., Derian, P.-J., Barnes, I. S., and Ninham, B. W., *J. Phys. Chem.* **91**, 3814 (1987).
34. Kaler, E. W., *in* "Modern Aspects of Small-Angle Scattering" (H. Brumberger, Ed.), p. 329. Kluwer Academic, Dordrecht, 1993.
35. Debye, P., and Bueche, A. M., *J. Appl. Phys.* **20**, 518 (1949).
36. Zhu, Z., Lin, M., Dagan, G., and Tomkiewicz, M., *Mat. Res. Soc. Symp. Proc.* **376**, 353 (1995).
37. Gradzielski, M., and Hoffmann, H., *in* "The Structure, Dynamics and Equilibrium Properties of Colloidal Systems" (D. M. Bloor and E. Wyn-Jones, Eds.), p. 427. Kluwer, Amsterdam, 1990.
38. Ashcroft, N. W., and Lekner, J., *Phys. Rev.* **145**, 83 (1966).
39. Bleier, A., and Cannon, R. M., *Mat. Res. Soc. Symp. Proc.* **73**, 71 (1986).